1   **Revision 1**

2   **Temperature-induced densification in compressed basaltic glass revealed by**

3   **in-situ ultrasonic measurements**

4   Man Xu[1,2], Zhicheng Jing[3*], Young Jay Ryu[1], Julien Chantel[4], James A. Van Orman[2], Tony Yu[1],

5   Yanbin Wang[1]

6   [1]Center for Advanced Radiation Sources, The University of Chicago, Chicago, IL 60637, USA

7   [2]Department of Earth, Environmental, and Planetary Sciences, Case Western Reserve University,

8   Cleveland, OH 44106, USA

9   [3]Department of Earth and Space Sciences, Southern University of Science and Technology,

10   Shenzhen, Guangdong, 518055, China

11   [4]University of Lille, CNRS, INRAE, Centrale Lille, UMR 8207 - UMET - Unité Matériaux et

12   Transformations, 59000 Lille, France

13   [*]Correspondence to: Z. Jing, jingzc@sustech.edu.cn

14

15   **Abstract**

16   Acoustic velocities of a model basalt glass (64 mol% $CaMgSi_2O_6$ + 36 mol% $CaAl_2Si_2O_8$)

17   were measured along different pressure (P)-temperature (T) paths. One set of experiments

18   involved isothermal compression-decompression cycles, performed at temperatures of 300 K,

19   641 K, 823 K, and 1006 K and pressures up to 12.2 GPa. The other set of experiments involved

20   constant-load heating-cooling cycles at temperatures up to 823 K and pressures up to 7.5 GPa.

21   Both sets of experiments were performed in a multi-anvil apparatus using a synchrotron-based

22   ultrasonic technique. Our results show that the glass compressed isothermally at 300 K (cold-

23   compression) displays anomalously decreasing compressional (V_P) and shear (V_S) wave

24   velocities with increasing pressure until ~8 GPa. Beyond 8 GPa, both V_P and V_S start to increase

25   sharply with pressure and irreversible densification of the glass occurred, producing large

26   hysteresis loops of velocities upon decompression. However, for the glass compressed

27   isothermally at increasingly higher temperatures (hot-compression), the velocity minima

28   gradually shift to lower pressures. At temperature close to the glass transition temperature T_g, the

29   velocity minima disappear completely, displaying a monotonic increase of velocities during

30   compression and higher V_P and V_S during decompression. In addition, constant-load heating-

31   cooling experiments show that velocities generally decrease slightly with increasing temperature,

32   but start to increase once heated above a threshold temperature (~650 K). During cooling the

33   velocities increase almost linearly with decreasing temperature, resulting in higher velocities

34   (~1.5-2.5% higher) when returned to 300 K. This implies that a temperature-induced

35   densification may have occurred in the glass at high pressures. Raman spectra on recovered

36   samples show that the hot-compressed and high-P heated glasses contain distinctly densified and

37   depolymerized structural signatures compared to the initial glass and the cold-compressed glass

38   below the velocity transition pressure P_T (~8 GPa). Such densification may be attributed to the

39   breaking of bridging oxygen bonds and compaction in the intermediate-range structure. Our

40   results demonstrate that temperature can facilitate glass densification at high pressures and point

41   out the importance of P-T history in understanding the elastic properties of silicate glasses.

42   Comparison with melt velocity suggests that hot-compressed glasses may better resemble the

43   pressure dependence of velocity of silicate melts than cold-compressed glasses, but still show

44   significantly higher velocities than melts. If the abnormal acoustic behaviors of cold-compressed

45   glasses were used to constrain melt fractions in the mantle low-velocity regions, the melt

2

46   fractions needed to explain a given velocity reduction would be significantly underestimated at

47   high pressures.

48

49   **Key words**: silicate glass, acoustic velocity, high pressure and high temperature, intermediate-

50   range structure, low-velocity regions

51

52   **1. Introduction**

53   The presence of silicate melts is believed to be the major reason for the seismically detected

54   low-velocity regions in the Earth's mantle (Anderson and Spetzler 1970; Williams and Garnero

55   1996; Kawakatsu et al. 2009; Hirschmann 2010; Schmerr 2012; Stern et al. 2015; Chantel et al.

56   2016; Debayle et al. 2020). These deep-seated partial melts may have played a critical role in

57   controlling chemical differentiation and heat transfer in the deep Earth. Depending on the density

58   contrast between silicate melts and the ambient mantle, melts can either migrate upwards or sink

59   into the deep interior (Stolper et al. 1981; Agee 1998; Sanloup 2016), resulting in divergent

60   geodynamical scenarios. Knowledge of the density is critical to understanding the dynamic

61   behavior of silicate melts, and both density and elastic properties (e.g., compressibility) are

62   essential to better constrain the melt fractions in the low-velocity regions of the mantle (e.g.,

63   Clark and Lesher, 2017; Takei, 2002) and to improve thermodynamic modelling of mantle

64   melting (e.g., Ghiorso, 2004).

65   While the high-pressure density of silicate melts can be directly measured using various

66   techniques including sink-float (Agee and Walker 1993; Agee 1998; Matsukage et al. 2005), X-

67   ray absorption (Sakamaki et al. 2010; Seifert et al. 2013; Malfait et al. 2014), shock compression

68   (Rigden et al. 1989; Asimow and Ahrens 2010; Thomas and Asimow 2013), and more recently

69   X-ray microtomography (Xu et al. 2020a), measurements of high-pressure acoustic velocities of

70   silicate melts are very challenging and limited. Until now, only two studies (Xu et al. 2018, 2022)

71   have reported sound velocity data measured directly on silicate melts along the diopside-

72   hedenbergite join at simultaneously high P-T conditions, using the ultrasonic technique in a

73   multi-anvil press. Considered as an alternative to silicate melts, silicate glasses have been chosen

74   in many studies as analogs for their melt counterparts to infer acoustic and elastic behaviors of

75   melts at high pressures (e.g., Aoki et al., 2020; Clark et al., 2016; Clark and Lesher, 2017; Liu

76   and Lin, 2014; Malfait et al., 2011; Meister et al., 1980; Murakami and Bass, 2011; Sakamaki et

77   al., 2014a; Sanchez-Valle and Bass, 2010; Suito et al., 1992; Wu et al., 2014). These studies have

78   revealed that many silicate glasses, especially polymerized glasses, exhibit an anomalous

79   velocity response to compression at room temperature, with acoustic velocities having a weak or

80   negative pressure dependence at relatively low pressures (usually from room pressure to a few

81   GPa) and a positive pressure dependence at higher pressures. For example, the acoustic velocity

82   of a basalt glass at high pressures has been determined by Liu and Lin (2014) using Brillouin

83   scattering spectroscopy in a diamond anvil cell and displays decreasing V_P and V_S with velocity

84   minima at about 2 GPa. This acoustic softening behavior in glasses has been used in some

85   studies (e.g., Clark and Lesher, 2017) to model melt velocities in the mantle low-velocity zones,

86   arguing for a very large velocity reduction due to the presence of partial melts. However,

87   whether the acoustic behaviors of glasses can be directly applied to their corresponding melts in

88   the Earth's mantle is still debated (Xu et al. 2018).

89   One may argue that the difference in velocities between melts and glasses may be caused by

90   temperature. Indeed, previous first-principles molecular dynamics (FPMD) simulations on

91   silicate glasses with different compression paths have demonstrated that cold-compressed glasses

4

92 at 300 K behave quite differently than hot-compressed glasses quenched from high pressure and

93 high temperature, with hot compression producing glasses with higher density, higher acoustic

94 velocity, and greater coordination numbers than cold compression (Ghosh et al. 2014; Ghosh and

95 Karki 2018). Acoustic velocities in the hot-compressed glasses also increase monotonically with

96 pressure in FPMD simulations, in contrast to the anomalous behavior of the cold-compressed

97 glasses (Ghosh and Karki 2018), suggesting that hot-compressed glasses may be better analogs

98 for high-pressure silicate melts. However, whether high temperature can substantially modify the

99 acoustic behavior of silicate glasses at high pressures and make them better mimic the melts has

100 not been examined experimentally.

101   Here we report in-situ ultrasonic measurements on a model basalt glass along different P-T

102 paths, including compression at room temperature (cold compression), compression at high

103 temperatures (hot compression), and heating-cooling experiments at fixed hydraulic-press loads

104 (heating-cooling at high P) to investigate the effect of temperature on glass acoustic properties.

105 Our results show that the acoustic behavior of the model basalt glass is strongly dependent on its

106 P-T path. Temperature-induced densification and structural modifications in the compressed

107 basaltic glass were observed above ~673 K, implying either an apparent negative thermal

108 expansion for basaltic glass at high P-T or a polymorphic transition in basaltic glass, similar to

109 those observed in silica glass (Mukherjee et al. 2001; Yokoyama et al. 2010; Guerette et al.

110 2018). It should be noted that the simplified model basalt composition used in this study does not

111 contain Fe and H_2O, which have been shown to significantly affect the structures and properties

112 of silicate glasses (e.g., Wu et al. 2014; Zhang et al. 2016). Future studies on more complex glass

113 compositions are needed to validate whether the temperature effects on model basalt glass at

114 high pressures observed in this study can be extended to natural systems.

115

2. Samples and Methods

117   Reagent-grade powders of MgO, $CaCO_3$, Al_2O_3, and SiO_2 were mixed in appropriate

118   proportions to produce the model basalt (MB, 64 mol% $CaMgSi_2O_6$-diopside + 36 mol%

119    $CaAl_2Si_2O_8$-anorthite) composition (NBO/T = ~0.94), and ground under ethanol for ~2 hrs. The

120   mixture was then dried and decarbonated at 1173 K in a high-temperature box furnace for ~24

121   hrs. The full release of CO_2 was confirmed by checking the weight of the mixture before and

122   after decarbonation. The decarbonated mixture was then fused at 1773 K for ~1 hr, and finally

123   quenched to glass. The fusion process was repeated twice to ensure homogeneity of the glass.

124   The resulting MB glass was transparent, bubble-free, and homogeneous, with a density of 2.767

125    $\pm$ 0.014 g/cm^3 measured by the Archimedes method. Cylindrical glass disks with outer diameter

126   of 1.8 mm were machined from the quenched glass chunks using a CNC-milling machine. The

127   top and bottom surfaces of the glass disks were polished to a roughness of less than 1 μm with

128   nearly perfect parallelism and were used as the samples for high-pressure ultrasonic

129   measurements.

130   The high-pressure experiments were performed in a 1000-ton large volume press with a

131   Kawai-type (T25) multi-anvil module (Wang et al. 2009) at the GSECARS beamline 13-ID-D of

132   the Advanced Photon Source, Argonne National Laboratory. The cell assembly is shown in

133   Supplementary Fig. 1. The experimental details have been described previously in (Xu et al.

134   2018, 2020b), and are only briefly summarized here. An $MgO-MgAl_2O_4$ octahedron with 14 mm

135   edge length was used as the pressure medium. A graphite sleeve, inserted into ZrO_2 thermal

136   insulators with an MgO X-ray window, was used as the heater. Well-polished molybdenum

137   buffer rod (BR) and backing plate (BP) were placed at the bottom and top of the sample,

6

138   respectively, to generate impedance and imaging contrast with the sample. The sample, BR, and

139   BP were separated from the heater by an Al_2O_3 sleeve. The pressure of the experiment was

140   determined by energy-dispersive X-ray diffraction of the pressure marker in the cell assembly,

141   consisting of a mixture of MgO and h-BN (MgO:BN = 3:1 by weight), using the high-

142   temperature equation of state (EOS) of MgO (Tange et al. 2009). Uncertainty in the determined

143   pressures mainly comes from the uncertainty in the EOS of MgO and is estimated to be about

144   10%. Temperature was monitored by a W5Re-W26Re thermocouple, and is accurate to ±10 K.

145   All sample temperatures reported in this study have been corrected to account for the

146   temperature gradient in the ultrasonic cell assembly, as calibrated by Xu et al. (2018).

147   The detailed procedure for ultrasonic measurements has been described in Jing et al. (2020).

148   A 10° Y-cut $LiNbO_3$ piezoelectric transducer with a resonant frequency of 50 MHz for

149   compressional (P)-waves and 30 MHz for shear (S)-waves was attached to the back of the

150   bottom tungsten carbide anvil. An arbitrary function generator was used to generate electrical

151   signals of sine waves in the frequency range of 20-60 MHz. The electrical signals were then

152   converted to P- and S-waves by the transducer. The converted elastic waves then traveled

153   through the bottom anvil and the cell assembly, and were reflected back at the anvil-buffer rod

154   (BR), BR-sample, and sample-backing plate (BP) interfaces. The reflected elastic waves were

155   received by the same transducer which converted them back to electrical signals that were

156   recorded by a digital oscilloscope at a sampling rate of 6.5×10^9 sample/s. Two-way travel time

157   through the sample was determined by the pulse-echo overlap method (Kono et al. 2012; Li and

158   Liebermann 2014; Jing et al. 2020) using the reflected signals from the BR-sample and sample-

159   BP interfaces. Uncertainty in travel time is within ±0.2 ns, corresponding to a relative

160   uncertainty of about 0.1%. Sample length was determined from radiographic imaging of the

161   sample by plotting the derivative of the image gray value versus pixel distances (Fig. 1a).

162   Uncertainty in sample length is within 3 pixels (1 pixel=1.77 μm), translating to a relative

163   uncertainty of less than 0.7%. The acoustic velocity was then calculated from the travel time and

164   sample length, with a total uncertainty of ~0.8%. Detailed analysis of the uncertainty is given in

165   Supplementary Materials. Examples of the sample image and ultrasonic signals for P- and S-

166   waves at 3.6 GPa and 823 K for the model basalt glass are shown in Fig. 1.
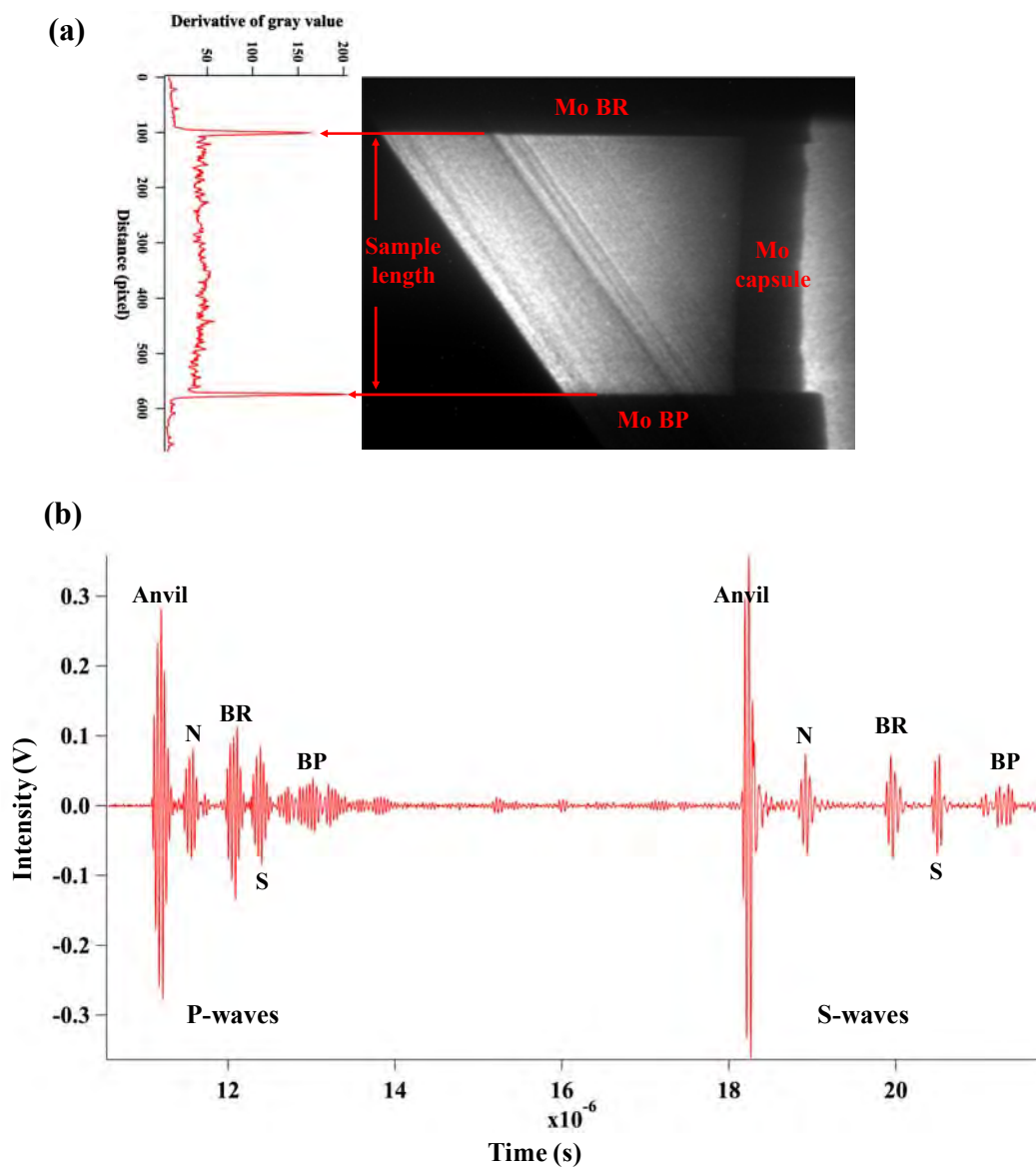

167

168   **Fig. 1** (a) X-ray radiographic image and (b) P-wave and S-wave ultrasonic signals for model basalt glass at 3.6 GPa

169   and 823 K. Mo - molybdenum, BR - buffer rod, BP - backing plate, N - noise, S - sample.

170   The experimental P-T paths are shown in Fig. 2. The P-T paths can be classified into two

171   types: (1) isothermal compression/decompression at room temperature (300 K, cold compression)

172   and high temperatures of 641 K, 823 K, and 1006 K (hot compression) (Fig. 2a); and (2)

173   heating/cooling at fixed hydraulic ram loads of 100 tons, 150 tons, 200 tons, and 250 tons (Fig.

174   2b). For cold compression, two experimental runs (T2545 and T2743) were performed. For run

175   T2545, the sample was compressed at room temperature up to 8.2 GPa, with data only collected

176   during compression. For run T2743, the sample was compressed to 12.2 GPa, with data collected

177   during both compression and decompression. For the isothermal hot compression runs (T2689,

178   T2690 and T2698), the sample was first compressed to ~20-30 tons (~0.8 GPa) at room

179   temperature to obtain clear ultrasonic signals for both P and S waves, as well as to make sure that

180   the heater and electrode were in good contact, and then the sample was heated to the target

181   temperatures (641, 823, or 1006 K), which are below or close to the glass transition temperature

182   (T_g = 1003 ± 15 K) for a model basalt glass of slightly different composition ($Di_{60}An_{40}$)

183   (Schilling et al. 2003). While keeping temperature constant, the pressure was slowly increased up

184   to about 8 GPa and then decreased to about 1 GPa, with data collected during both compression

185   and decompression (Fig. 2a). For heating-cooling experiment (T2463), the sample was first

186   compressed at room temperature to a load of 100 tons, at which a heating-cooling cycle was

187   performed. The temperature was increased up to 823 K and then decreased to room temperature

188   at a heating/cooling rate of ~50 K/min. The acoustic velocities were measured along both heating

189   and cooling in steps of every ~200 K, which took about ~1 hr to complete. Three additional

190   heating-cooling cycles were performed at 150, 200, and 250 tons, respectively, following the

191   same measurement procedure as the first heating cycle. The four cycles correspond to a pressure

192   range of 1.2 to 7.5 GPa and a temperature range of 300 to 823 K (Fig. 2b). A summary of all

193   experimental runs is given in Table 1.
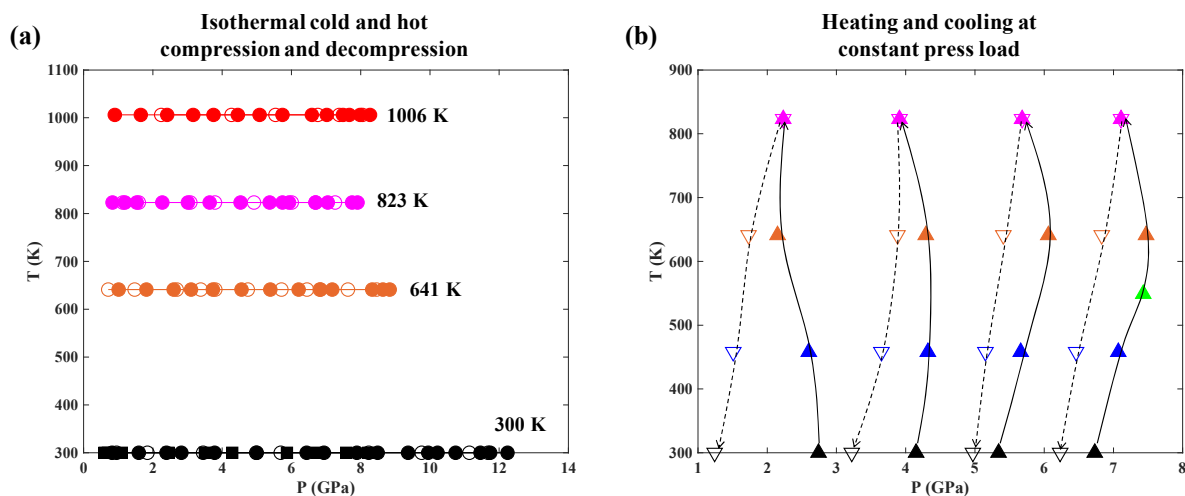
194

195   **Fig. 2** Experimental P-T paths for (a) isothermal cold and hot compression/decompression experiments, and (b)

196   heating/cooling experiment at constant press loads. Solid symbols in (a) indicate compression and open symbols

197   indicate decompression. Black circles are for cold run T2743 where both compression and decompression data were

198   collected and black squares are for cold run T2545 where only compression data were collected. Orange, magenta,

199   and red are for isothermal runs T2689, T2690, and T2698 along isotherms of 641 K, 823 K, and 1006 K,

200   respectively. Solid black curves in (b) indicate heating and dashed black curves indicate cooling. Data collected

201   during heating are shown as upward-pointing triangles and during cooling shown as downward-pointing triangles.

202   Black – 300 K, blue – 458 K, green – 549 K, orange – 641 K, magenta – 823 K, and red – 1006 K. At 823 K for

203   heating-cooling experiment, the data points can be either considered as the end of heating or the start of cooling, so

204   they are shown together as overlapped data points.

205

206   **Table 1** Summary of all experimental runs along different P-T paths

Run no.	Experimental type	Max P (GPa)	Max T (K)	Velocity transition pressure P_T (GPa)	Elastic anomaly extent in V_P (m/s)	Elastic anomaly extent in V_S (m/s)

10

T2545	Cold compression	8.2	300	8	443	305
T2743	Cold compression	12.2	300	8	482	396
T2689	Hot compression	8.8	641	5-6	275	241
T2690	Hot compression	7.9	823	2-3	44	89
T2698	Hot compression	8.3	1006	None	None	None
T2364	Heating-cooling at fixed loads	7.5	823			

207   Max P and Max T represent the maximum pressure and maximum temperature reached for the experimental run,

208   respectively. The velocity transition P indicates the pressure where the elastic anomaly occurs, resulting in a velocity

209   minimum as a function of pressure. Elastic anomaly extents are calculated from the difference between the starting

210   velocity value at ~1 GPa and the velocity minimum at the transition pressure P_T.

211   The recovered samples from all experiments were mounted in epoxy, sectioned, and polished

212   for Raman spectroscopy analysis. Raman spectra were acquired using a micro-confocal Raman

213   system in the backscattering geometry at GSECARS (Holtgrewe et al. 2019), with a 20×

214   objective lens and a 532-nm excitation laser, collected in the wavenumber range from 10 cm^{-1} to

215   1300 cm^{-1}. The exposure time for each acquisition was 10 s, and 18 repeated acquisitions were

216   averaged to obtain a clean spectrum. A polynomial background was subtracted from the raw

217   Raman spectra using the software Fityk (Wojdyr 2010), and the intensity of each spectrum was

218   normalized with respect to the maximum intensity. The Raman spectra for initial starting glass

219   and all recovered samples are compared in Fig. 3. No crystallization has been found in all

220   recovered samples, confirming that the samples remained in glass state at high P-T conditions.

221   The recovered glass samples were unfortunately too small (<1 mm, ~1-2 mg in weight) for

222   density to be accurately determined by the Archimedes method.

223

224
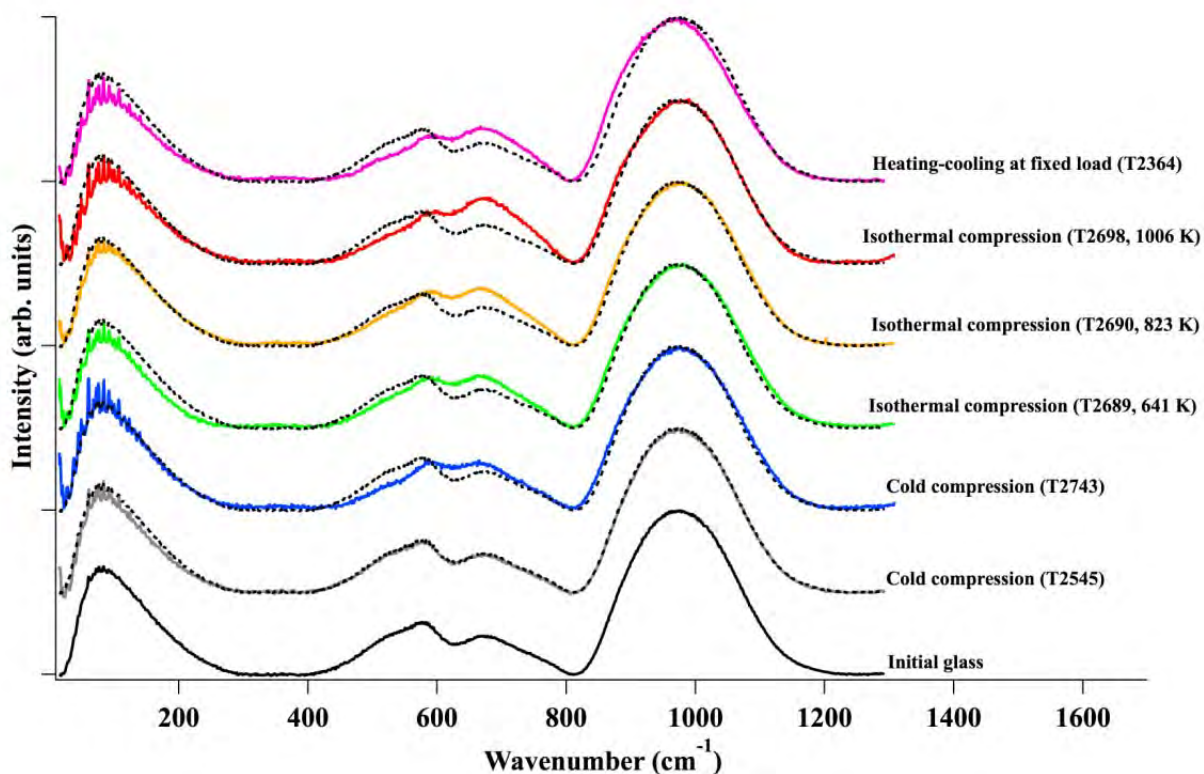
Fig. 3 Raman spectra for the initial starting model basalt glass (black) and the recovered samples, including cold-compression experiment T2545 (gray), cold-compression experiment T2743 (blue), isothermal compression at 641 K (green), isothermal compression at 823 K (orange), isothermal compression at 1006 K (red), and heating-cooling experiment at fixed loads (magenta). For better comparison, the spectrum for the initial glass (black dashed spectrum) is overlapped with the spectra of the recovered samples.

3. Results

3.1 Isothermal compression and decompression

The experimental conditions and measured acoustic velocity data are given in Supplementary Table 1. The P- and S-wave velocity (V_P and V_S, respectively) as a function of pressure for the two cold-compression runs (black circles and squares) are shown in Fig. 4a and 4b, respectively. During cold compression, both V_P and V_S of the glass decrease with pressure until ~8 GPa, after which they start to increase sharply with pressure. This reversal of pressure dependence of

12

238   velocity is similar to the elastic anomaly observed in silica glass (Huang et al. 2004; Deschamps

239   et al. 2009) and other polymerized silicate glasses (Tkachev et al. 2005; Sonneville et al. 2013;

240   Sakamaki et al. 2014b), although the transition pressures (hereafter referred to as P_T) are

241   different. During decompression from ~12 GPa, a large open hysteresis loop is observed and the

242   velocities during decompression are significantly higher than those during compression (Fig. 4),

243   indicating that the glass has been permanently densified. The density of the cold-compressed

244   glass (Fig. 4c) can be calculated by integrating the measured velocities as a function of pressure,

245   assuming that the deformation is elastic and isotropic (e.g., Liu and Lin, 2014; Sanchez-Valle

246   and Bass, 2010; Wu et al., 2014) ,

247   $\rho - \rho_0 = \int_{P_0}^{P} \frac{1}{V_B^2} dP = \int_{P_0}^{P} \frac{1}{V_P^2 - 4V_S^2/3} dP$ (1)

248   where V_B is the bulk velocity and ρ_0 is the initial room-pressure density for the glass determined

249   by the Archimedes method. The calculated density confirms that the glass above P_T has been

250   permanently densified by ~3.7%, resulting in higher density during decompression (Fig. 4c). It

251   should be noted that the density calculated using Eqn. (1) may underestimate the degree of

252   permanent densification above ~8 GPa, as the effect of irreversible structural changes on the

253   glass density is not accounted for in Eqn. (1). For run T2545 where the sample was cold-

254   compressed to ~8.2 GPa, close to P_T, the recovered sample has almost identical Raman spectrum

255   as the initial starting glass (Fig. 3), suggesting that compression of glass to pressures lower than

256   P_T is fully recoverable. In contrast, recovered sample from run T2743 compressed up to ~12 GPa

257   shows significantly different Raman spectrum in the region of 400-800 cm^{-1} than the initial glass

258   (Fig. 3), consistent with the permanent densification of the glass.

259   The velocities for three hot-compression runs at 641 K (orange), 823 K (magenta), and 1006

260   K (red) are also shown in Fig. 4. Several observations can be made by comparing the velocities

261 along different isotherms (Fig. 4). First, with increasing temperature, P_T shifts to lower pressures

262 from ~8 GPa at 300 K to ~5-6 GPa at 641 K and then to ~2-3 GPa at 823 K until it totally

263 disappears at 1006 K. This implies that permanent densification of the glass begins to occur at

264 progressively lower pressure when temperature is increased. Second, the extent of the elastic

265 anomaly along compression, defined as the difference between the velocity minimum and the

266 initial velocity at ~0.8-1 GPa, reduces with increasing temperature. Third, the hysteresis loop

267 between compression and decompression narrows at higher temperatures. All these observations

268 have been summarized in Table 1. The recovered samples from all high-T isothermal runs show

269 different Raman spectra compared to the initial glass (Fig. 3), but similar general features with

270 each other as well as with the permanently densified cold-compressed glass recovered from

271 compression to ~12 GPa. However, the intensity of the Raman band centered at ~670 cm^{-1}

272 increases prominently with increasing temperature, suggesting some irreversible structural

273 change has been induced by temperature at high pressures (Fig. 3 and Section 4.1 for more

274 details).

275

14

(a)

(b)

(c)

276

15
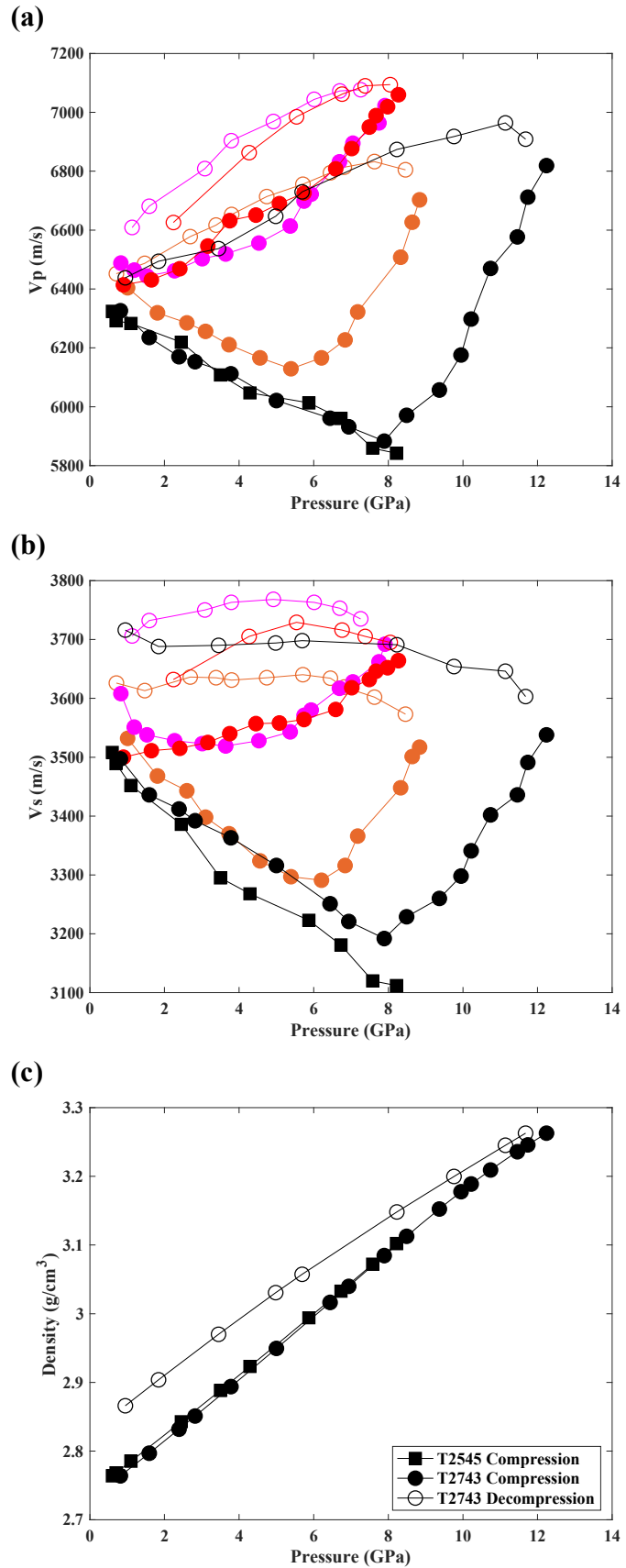
277   **Fig. 4** V_P (a) and V_S (b) as a function of pressure for model basalt glass along different isotherms. Panel (c) is the

278   calculated density for the two cold-compression runs by integrating the measured velocities as a function of pressure

279   using the initial glass density determined by the Archimedes method. Solid and open symbols are data collected

280   along compression and decompression, respectively, with different colors representing different isotherms. Black –

281   300 K, orange – 641 K, magenta – 823 K, and red – 1006 K. The black squares are data from the cold-compression

282   run T2545.

283

284   *3.2 Heating and cooling at fixed loads*

285   The V_P and V_S for model basalt glass measured in the heating-cooling experiment at fixed

286   press loads (run T2364) are shown as a function of pressure in Fig. 5a and 5b, respectively, and

287   also as a function of temperature in Fig. 5c and 5d, respectively. It can be clearly seen from Fig.

288   5 that the velocities (both V_P and V_S) follow different paths for heating and cooling. During

289   heating, the velocities generally decrease with temperature until a certain point between ~641

290   and 823 K, where the velocities start to increase with temperature. During cooling, the velocities

291   increase with decreasing temperature almost linearly, resulting in higher velocities (by ~1.5-

292   2.5%) than those measured during heating (Fig. 5), implying possible structural densification

293   behaviors in the glass even below the glass transition temperature. In addition, the subsequent

294   heating cycles below 641 K seem to follow or fall slightly below the previous cooling cycles,

295   suggesting that some amount of densification and structural change that is induced by each

296   heating cycle above 641 K may be partially retained upon further compression and heating.

297   Compared with isothermal runs at high pressures (Fig. 4), the heating experiments show a

298   decrease of velocity until ~641 K and then a marked increase at ~641-823 K. As a result, the

299   velocity of the glass at 673 K during heating is generally lower than at 300 K before heating (Fig.

300   5). In contrast, the isothermal experiments show a decrease of the velocity transition pressure P_T

301   with increasing temperature, resulting in higher velocities for the 641 K isotherm than the 300 K

16

302   isotherm above P_T (Fig. 4). This observation suggests that the temperature response of glass

303   velocity is also strongly dependent on the P-T paths (isothermal compression vs. isobaric

304   heating).
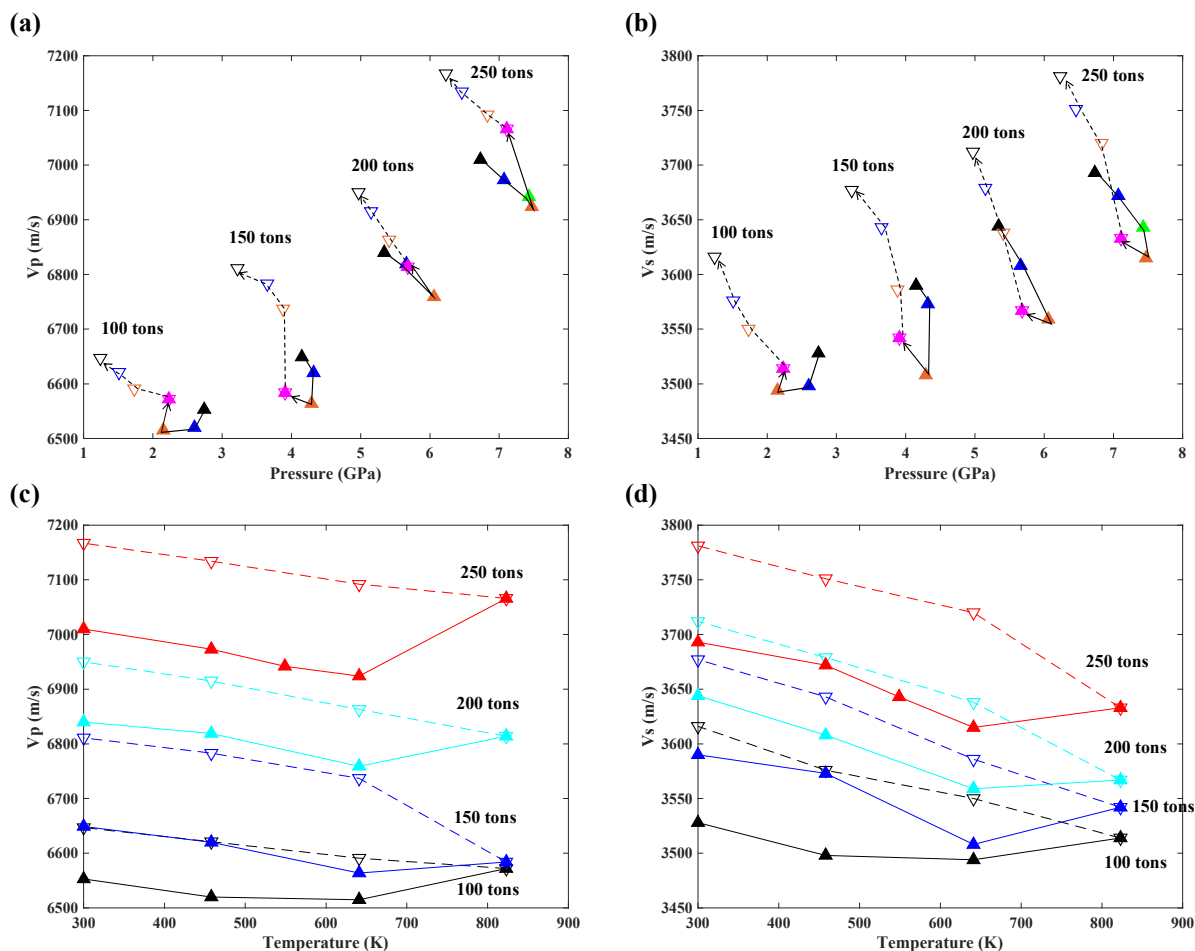
305

306   **Fig. 5** (a) and (b) are V_P and V_S as a function of pressure for the heating-cooling experiment at different fixed press

307   loads. Solid upward-pointing triangles and solid lines represent heating, while open downward-pointing triangles

308   and dashed lines represent cooling. Different marker colors represent different temperatures (black – 300 K, blue –

309   458 K, green – 549 K, orange – 641 K, magenta – 823 K). (c) and (d) are the same dataset plotted as a function of

310   temperature for V_P and V_S, respectively. Different colors indicate different press loads (black – 100 tons, blue – 150

311   tons, cyan – 200 tons, red – 250 tons).

312

313   **4. Discussion**

17

314   All the above observations indicate that temperature can substantially modify the acoustic

315   behaviors of silicate glasses under compression, and that the glass velocity is strongly dependent

316   on its P-T path. The anomalous acoustic behaviors found previously in cold-compressed silicate

317   glasses (e.g., Clark et al., 2016; Liu and Lin, 2014; Sanchez-Valle and Bass, 2010) do not seem

318   to fully extend to hot-compressed glasses and should not be directly applied to silicate melts in

319   the Earth's mantle without accounting for the effect of temperature. The lack of direct in-situ

320   structural measurements in the present study precludes a detailed atomic-level understanding of

321   the complex acoustic and elastic behaviors of silicate glasses. Nevertheless, some discussion is

322   given below by comparing our Raman data of recovered glasses with those from relatively well-

323   studied silica (SiO_2) glass in the literature. The elastic and structural properties of SiO_2 glass

324   have been extensively studied and may be used as prototypes to explain the behaviors in silicate

325   glasses. For SiO_2 glass, it has been proposed that shrinking in Si-O-Si angle (Deschamps et al.

326   2009) and Si void structural change (Kono et al. 2022) may be the cause for the velocity minima

327   observed during room-temperature compressions.

328

329   *4.1 Effect of temperature on glass velocity and compression mechanism*

330   Room-pressure Brillouin scattering studies (Askarpour et al. 1993; Schilling et al. 2003) and

331   density measurements (Lange 1997) on silicate glasses have shown that the velocity (both V_P

332   and V_S) and density for room-pressure silicate glasses decrease almost linearly with temperature

333   in both the glassy state and the supercooled liquid state, with a sharp increase of the temperature

334   derivative at the glass transition temperature T_g. Our heating-cooling results also show linear

335   decreases of velocity with increasing temperature for measurements made during cooling (Fig. 5).

336   However, the change of temperature dependence of velocity below T_g during heating in our

18

337 high-pressure experiments (Fig. 5) has not been observed for room-pressure measurements

338 (Schilling et al. 2003). These observations suggest that the effect of temperature on the acoustic

339 behavior of silicate glasses is multifaceted and likely coupled with pressure. On the one hand, the

340 acoustic behavior measured during cooling (velocity decreases with temperature) is similar to

341 that observed in most crystalline silicates. This can be explained by the direct effect of

342 temperature on acoustic velocities through the anharmonicity of lattice vibrations. On the other

343 hand, temperature enhances the kinetics of structural reorganization of glasses at high pressures,

344 and it is likely that glasses under compression may undergo structural changes after passing a

345 threshold temperature at ~641-823 K, resulting in permanent densification of the glass at much

346 lower pressures than cold compression.

347   The Raman spectra of the recovered samples for hot-compressed glasses (T2689, T2690 and

348 T2698) and the glass that experienced multiple heating cycles (T2364) are indeed distinct from

349 that of the initial glass and cold-compressed glass below P_T (Fig. 3). For all Raman spectra, they

350 can be divided into three frequency regions. The broad band at 10-250 cm^{-1} corresponds to the

351 boson region (Neuville et al. 2014). The region from 250 to 800 cm^{-1} involves bending vibrations

352 of T-O-T linkages (T=Si, Al) in silicate glasses (McMillan 1984; Neuville et al. 2014; Moulton

353 et al. 2019), and the region from 800 to 1200 cm^{-1} is associated with the anti-stretching mode of

354 SiO_4 and AlO_4, which can be distributed into Q^n species (where n represents the number of

355 bridging oxygens per TO_4) (McMillan 1984; Shimoda et al. 2005). Raman spectra of the initial

356 glass and cold-compressed glass below P_T (T2545) are virtually identical (Fig. 3), indicating that

357 the structure of the cold-compressed glass up to ~8 GPa is fully recovered to ambient conditions.

358 In contrast, all the other recovered samples show significantly different spectra when compared

359 with the initial glass, suggesting permanent structural changes have occurred in these glasses.

19

360 All the glass spectra show two distinct maxima which are centered around 580 and 670 cm^{-1}

361 (Fig. 3). For the initial glass and cold-compressed glass up to 8.2 GPa, the 580 cm^{-1} band is more

362 intense than the 670 cm^{-1} band, while the relative intensities are reversed for the hot-compressed

363 glasses and heated glass at high P, with the intensity of the 670 cm^{-1} band increasing with

364 temperature. In addition, the 580 cm^{-1} band also shifts to a higher wavenumber (~590 cm^{-1}) for

365 the hot-compressed and heated glasses, and the small shoulder observed at ~500 cm^{-1} for the

366 initial glass and cold-compressed glass below ~8 GPa becomes less pronounced for hot-

367 compressed and high-P heated glasses. These observations are consistent with previous Raman

368 studies on anorthite glass with permanent densification features (Reynard et al. 1999; Moulton et

369 al. 2019). According to high-pressure Raman studies on glasses in the Di-An join (Moulton

370 2016), the ~580 cm^{-1} band may correspond to Si-O-Si vibrations within polymerized units as

371 assigned in An glass (Daniel et al. 1995; Mysen and Toplis 2007), and may also involve

372 contributions from the breathing vibration associated with tetrahedral ring structures (Galeener

373 and Geissberger 1983). The ~670 cm^{-1} band corresponds to Si-O-Si vibrations within

374 depolymerized units as assigned in Di glass (Moulton 2016). Within the polymerized units for

375 An glass, the 580 cm^{-1} band may be interpreted as the breathing modes of four-membered

376 tetrahedral rings at 500 cm^{-1} (D_1) and three-membered tetrahedral rings at 587 cm^{-1} (D_2)

377 (Moulton et al. 2019). Thus, the decrease of the intensity of the 500 cm^{-1} shoulder and shift of

378 the 580 cm^{-1} band to a higher wavenumber suggest that the densification of model basalt glass at

379 high P-T may involve a change in tetrahedral ring statistics (Reynard et al. 1999; Moulton et al.

380 2019), favoring smaller rings and less open structures, which has been shown to result in a

381 reduction of the elastic anomaly (Sonneville et al. 2013). In addition, the variation of intensities

382 of the ~580 and 670 cm^{-1} bands for hot-compressed and high-P heated glasses may suggest that

383   compression in the depolymerized structural units (e.g., increase of the 670 cm^{-1} band) becomes

384   more and more important for densified glasses at high P-T (Fig. 3).

385   The main band at ~960 cm^{-1} for the hot-compressed glasses remain more or less unchanged

386   compared to the initial glass (Fig. 3). However, the glass recovered from the heating-cooling

387   experiment has a slightly negative shift in the main band, implying that some amount of the

388   structural change related to the Q^n species is retained to ambient conditions (Kubicki et al. 1992;

389   Sonneville et al. 2012; Moulton et al. 2016). This shift indicates an increase of the Q^n species in

390   population with n=0 and decrease in populations with n=3 and 4, suggesting that the heated glass

391   at high P is depolymerized and densified due to compression and heating, possibly through

392   breaking of the bridging oxygen bonds and compaction of voids in the intermediate range

393   structure (Wang et al. 2014). Our Raman results show that even though the highest pressure

394   reached (~7.5 GPa) for the heated glass is lower than that of the cold-compressed glass before

395   the transition pressure (~8.2 GPa), the combination of heating and compression produces a more

396   densified glass.

397   Progressive shift of the elastic anomaly (velocity minimum) to lower pressure and a decrease

398   in the extent of the elastic anomaly with increasing depolymerization has been observed in

399   sodium aluminosilicate glasses with different NBO/T under pressure (Sonneville et al. 2013) as

400   well as in silica glass as a function of the permanent densification ratio (Sonneville et al. 2012)

401   and through thermally-induced densification (Guerette et al. 2015, 2018). These suggest that

402   high temperature facilitates structural compaction, depolymerization and densification of model

403   basalt glass under compression, resulting in its progressive loss of the velocity minimum with

404   increasing temperature as observed in Fig. 4.

405   For silica glass, it has been shown that temperature can facilitate its densification at high

406   pressures and elevate its acoustic velocity compared to the room-temperature compressed value

407   (Hofler and Seifert 1984; Yokoyama et al. 2010; Guerette et al. 2015). For example, Yokoyama

408   et al. (2010) measured the elastic wave velocities of a silica glass at simultaneous high pressure

409   and high temperature and found that the velocities measured at high P-T are higher than those

410   measured during room-temperature compression, due to an increase in density with temperature.

411   This implies an apparent negative thermal expansion for silica glass at high pressures

412   (Yokoyama et al. 2010). Using high-pressure quench experiments, Guerette et al. (2015)

413   demonstrated that the densification of silica glass strongly depends on temperature, with the high

414   P-T conditions being much more efficient in increasing the density than just cold compression

415   without heating, and that temperature can help eliminate the elastic anomalies observed in silica

416   glass. Thermally-induced polyamorphic transitions between high-density amorphous (HDA)

417   phase and low-density amorphous (LDA) phase in silica glass at high pressures has also been

418   reported (Mukherjee et al. 2001; Guerette et al. 2018). These distinct behaviors between cold-

419   compressed and high P-T silica glasses are also supported by the total structure factor S(q)

420   measured by X-ray diffraction (Inamura et al. 2004; Guerette et al. 2015). The first sharp

421   diffraction peak (FSDP) position of S(q), which is related to the intermediate-range order of the

422   network (Elliott 1991; Sakamaki et al. 2014b), increases with temperature to higher q values in a

423   specific temperature-pressure range, indicating that the intermediate-range structure of silica

424   glass is thermally densified at high pressures (Inamura et al. 2004; Katayama and Inamura 2005).

425   Meanwhile, contrary to the broadening and decrease in intensity of the FSDP in the room-

426   temperature compressed silica glass (Tan and Arndt 1999; Benmore et al. 2010; Sato and

427   Funamori 2010), the FSDP of high P-T silica glass narrows and its intensity does not change

22

428   much with pressure (Inamura et al. 2004; Guerette et al. 2015), suggesting that compression

429   disrupts the intermediate-range structures to a more chaotic size distribution whereas heating

430   homogenize the distribution. A similar narrowing and temperature dependence of FSDP for high

431   P-T jadeite glass and GeO_2 glass have also been observed by in-situ X-ray structural

432   measurements (Shen et al. 2007; Sakamaki et al. 2014a).

433   It is likely that model basalt glass at high P-T conditions may have gone through similar

434   structural densification as observed in silica glass (Inamura et al. 2004) and demonstrated in our

435   Raman spectra. Such densification may be responsible for the higher acoustic velocities observed

436   in the hot-compressed glasses than in the cold-compressed glasses, as well as the reduction of the

437   elastic anomaly with increasing temperature, through depolymerization and modification of the

438   glass structure (Fig. 4). Based on our velocity measurements, this thermally induced

439   densification in compressed silicate glasses likely happens during heating when temperature

440   reaches ~200-300 K below the T_g of the glass (Fig. 5). In addition, the densified structure may be

441   partially retained during cooling and further compression and decompression. The subsequent

442   heating cycles after some additional compression in our heating-cooling experiment likely

443   produced further densification, resulting in permanent densification of the intermediate-range

444   structure of the glass (Fig. 3).

445

446   *4.2 Comparison with silicate melt*

447   In order to further investigate whether hot-compressed glass or heated glass at high P can

448   better mimic the acoustic behavior of the corresponding melt than the cold-compressed glass or

449   not, we compare the velocity of model basalt glass and melt in Fig. 6. Currently, no direct

450   measurements of the sound velocity of model basalt melt are available. However, shock

451   experiments have been carried out on model basalt melt (Asimow and Ahrens 2010) and provide

452   its equation of state that can be used to calculate the sound velocity of model basalt melt along its

453   adiabat at high pressures.

454   As can be seen in Fig. 6a, first, the model basalt glass velocity, regardless of its P-T path, are

455   all significantly higher than the velocity of the melt; and second, the smoother pressure

456   dependence in the hot-compressed and high-P heated glass without elastic anomaly is more

457   consistent with that observed in melt. This indicates that hot-compressed glass may provide

458   closer analog for the melt at high pressures in terms of the pressure dependence of elastic

459   properties than cold-compressed glass, similar to the conclusion drawn from first-principle

460   simulations (Ghosh et al. 2014).

461   Previous studies on silicate melts have shown that additional compression mechanisms are

462   available to silicate melts, in addition to the internal energy contribution which predominantly

463   controls the compression of crystals through the reduction of mean atomic distance (Richet and

464   Neuville 1992; Schilling et al. 2003; Jing and Karato 2011; Xu et al. 2018). Such mechanisms

465   have been studied in detail in (Jing and Karato 2011) and the difference between melt and

466   crystal/glass was demonstrated to be due to the greater entropy of melt. Using a hard-sphere

467   model of silicate melts, (Jing and Karato 2011) showed that the kinetic energy related to the free

468   motion of melt components (such as MgO, SiO_2, etc.) considered as hard spheres is a significant

469   contribution to the free energy of the system and thus would be an important mechanism for melt

470   compression. This configurational entropy contribution to compression can also quantitatively

471   explain the much higher compressibility observed in melt than that in glass and crystal (Jing and

472   Karato 2011), and for model basalt melt this configurational compressibility has been estimated

473   to account for ~48% of its total compressibility at room pressure (Schilling et al. 2003).

24

474   Similarly, the much lower velocity of melt than that in crystal and glass is also believed to result

475   from the entropic effect (Xu et al. 2018).

476   Such a configurational contribution to compression, however, is not fully available in

477   glasses as their atomic configurations are kinetically frozen at the time scales of laboratory

478   measurements. Therefore, the measurements on glass can only reflect the energetic contribution

479   of a particular frozen configurational state which strongly depends on the thermal history of the

480   glass (Askarpour et al. 1993). For cold-compressed glass, due to the high kinetic hindrance to

481   structure change, compression is mostly accommodated by adjusting the intermediate-range

482   structures through topological rearrangements such as changes in bond angles and ring structures

483   (Hemley et al. 1986; Huang et al. 2004; Deschamps et al. 2009). However, compression at higher

484   temperatures or heating of the glass to ~200-300 K below the T_g homogenize the intermediate

485   structure and densify the glass to remove this effect (Fig. 4), which is likely because that high

486   temperature help reduce the kinetic barrier and increase the configurational space, making the

487   high-temperature glass more easily to be densified with pressure without the need for much

488   topological rearrangements in the intermediate-range structures. This is consistent with first-

489   principle simulations on silicate glasses (Ghosh et al. 2014; Ghosh and Karki 2018), showing

490   that in the low-pressure range (0-10 GPa), smooth increase in bond distance and coordination

491   occurs in the hot-compressed glass, while both Si and Al in cold-compressed glass display

492   mainly topological changes without significantly affecting the average bond distance and

493   coordination. In addition, NMR spectra on aluminosilicate glasses also show that highly

494   coordinated Al species increase with glass fictive temperatures (Stebbins et al. 2008), implying

495   that coordination changes may occur more easily for high-temperature glasses. All these

496   observations, therefore, suggest that high-temperature compressed silicate glass or

497 heated/annealed glass at high P may be a closer analog for high-pressure melt than cold-

498 compressed glass in terms of both structure and properties, although the high P-T glass may still

499 not be able to fully capture all the configurational contributions to compression that are

500 important in high-temperature melt, as the high P-T glass below T_g is still more kinetically

501 sluggish in structural changes in response to pressure than the high P-T melt. It should be

502 emphasized that glass, as a metastable rather than thermodynamically stable phase, has structure

503 and properties that are dependent on the sample preparation conditions and subsequent

504 measurement conditions, such as temperature, pressure, shear stress, heating/cooling rate,

505 compression/decompression rate, measurement timescale, etc. Caution should be taken when

506 applying or extrapolating glass properties to melt in Earth and planetary interiors.
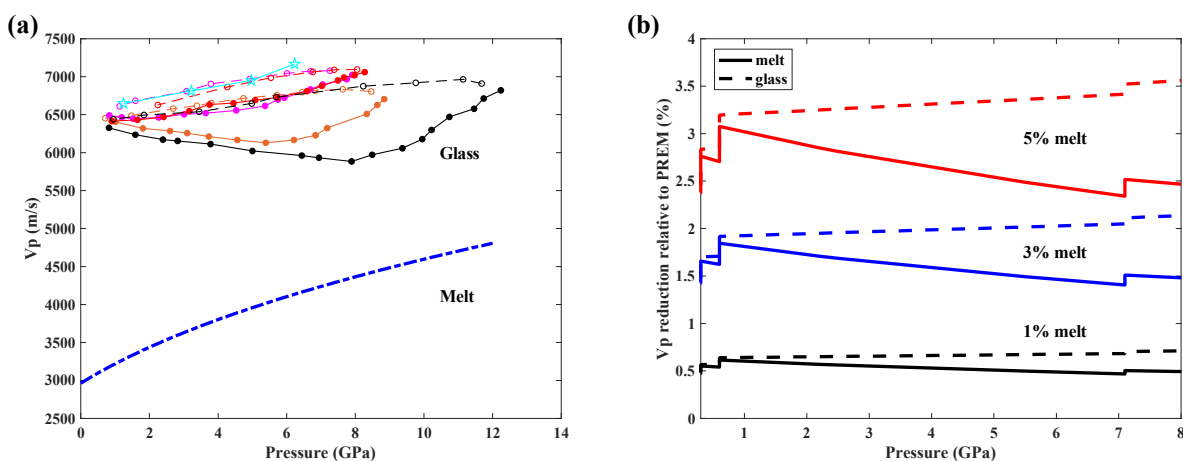
507

508 **Fig. 6 (a)** Comparison of the P-wave velocity (Vp) of model basalt glass from different P-T paths with that of model

509 basalt melt. The cold-compressed (black) and hot compressed (orange – 641 K, magenta – 823 K and red – 1006 K)

510 data for model basalt glass are plotted as the same symbols in Fig. 4. The cyan stars represent the data for the heated

511 glass at each fixed press load and 300 K after experiencing the heating-cooling cycle. The thick blue dash-dot curve

512 is the calculated velocity profile for model basalt melt based on the shock experimental results from (Asimow and

513 Ahrens 2010). (b) Vp reduction relative to the PREM model (Dziewonski and Anderson 1981) as a function of

514 pressure and melt fraction. Solid curves are calculated based on the EOS of model basalt melt (Asimow and Ahrens

515 2010). Dashed curves are calculated based on the cold-compression results of model basalt glass in this study, with

516   an anchored room-pressure velocity same as that of the model basalt melt (See calculation details in Supplementary

517   Materials). Black, blue and red represent 1%, 3% and 5% melt fraction, respectively.

518

Implications

520   Our study has clearly shown the distinct acoustic behaviors between cold-compressed and

521   hot-compressed/high-P heated glass, and pointed out the importance of temperature during

522   compression in order to fundamentally understand the behavior of silicate glasses. Since the

523   measured acoustic velocities on silicate glasses are unrelaxed, they cannot be directly compared

524   with seismic wave velocities which are measured at much lower and relaxed frequency to

525   constrain the composition and structure of possible melt layers in the Earth's interior. Cold-

526   compressed glasses are by no means good analogs for high P-T melt in the Earth's interior. Thus,

527   it would be inappropriate to use the anomalous pressure dependence of acoustic velocities

528   observed in various silicate glasses compressed at room temperature to approximate the velocity

529   of silicate melts as in previous models and experimental studies (e.g., Liu and Lin 2014; Clark et

530   al. 2016; Clark and Lesher 2017). Using the acoustic behavior of cold-compressed silicate

531   glasses can result in a significant underestimate of the melt fractions needed to explain a given

532   velocity reduction observed seismically, especially at high pressures (Fig. 6b). The high-

533   temperature compressed glasses may better mimic the pressure dependence of velocity in melts,

534   but are unlikely to fully capture the configurational properties that are important to melts.

535

Acknowledgements

27

540   Laboratory. GSECARS is supported by the National Science Foundation-Earth Sciences (EAR-

541   1634415) and Department of Energy - Geosciences (DE-FG02-94ER14466). This work used

542   resources of the Advanced Photon Source, a U.S. Department of Energy (DOE) Office of

543   Science User Facility operated for the DOE Office of Science by Argonne National Laboratory

544   under Contract No. DE-AC02-06CH11357. Use of the GSECARS Raman Lab System was

545   supported by the NSF MRI Proposal (EAR-1531583).

546

547   **References**

548   Agee, C.B. (1998) Crystal-liquid density inversions in terrestrial and lunar magmas. Physics of

549   the Earth and Planetary Interiors, 107, 63–74.

550   Agee, C.B., and Walker, D. (1993) Olivine flotation in mantle melt. Earth and Planetary Science

551   Letters, 114, 315–324.

552   Anderson, D.L., and Spetzler, H. (1970) Partial melting and the low-velocity zone. Physics of the

553   Earth and Planetary Interiors, 4, 62–64.

554   Aoki, K., Sakamaki, T., Ohashi, T., Ikeda, O., and Suzuki, A. (2020) Effects of alkali and

555   alkaline-earth cations on the high-pressure sound velocities of aluminosilicate glasses.

556   Physics and Chemistry of Minerals, 47, 28.

557   Asimow, P.D., and Ahrens, T.J. (2010) Shock compression of liquid silicates to 125 GPa: The

558   anorthite-diopside join. Journal of Geophysical Research: Solid Earth, 115.

559   Askarpour, V., Manghnani, M.H., and Richet, P. (1993) Elastic Properties of Diopside, Anorthite,

560   and Grossular Glasses and Liquids: A Brillouin Scattering Study up to 1400 K. Journal of

561   Geophysical Research, 98, 17683–17689.

562   Benmore, C.J., Soignard, E., Amin, S.A., Guthrie, M., Shastri, S.D., Lee, P.L., and Yarger, J.L.

563   (2010) Structural and topological changes in silica glass at pressure. Physical Review B -

564   Condensed Matter and Materials Physics, 81, 1–5.

565   Chantel, J., Manthilake, G., Andrault, D., Novella, D., Yu, T., and Wang, Y. (2016)

566   Experimental evidence supports mantle partial melting in the asthenosphere. Science

567   advances, 2, e1600246.

568   Clark, A.N., and Lesher, C.E. (2017) Elastic properties of silicate melts: Implications for low

569   velocity zones at the lithosphere-asthenosphere boundary. Science Advances, 3, e1701312.

570   Clark, A.N., Lesher, C.E., Jacobsen, S.D., and Wang, Y. (2016) Anomalous density and elastic

571   properties of basalt at high pressure: Reevaluating of the effect of melt fraction on seismic

572   velocity in the Earth's crust and upper mantle. Journal of Geophysical Research: Solid Earth,

573   121, 4232–4248.

574   Daniel, I., Gillet, P., Poe, B.T., and Mcmillan, P.F. (1995) In-situ High-Temperature Raman

575   Spectroscopic Studies of Aluminosilicate Liquids. Physics and Chemistry of Minerals, 22,

576   74–86.

577   Debayle, E., Bodin, T., Durand, S., and Ricard, Y. (2020) Seismic evidence for partial melt

578   below tectonic plates. Nature, 586, 555–559.

579   Deschamps, T., Martinet, C., de Ligny, D., and Champagnon, B. (2009) Elastic anomalous

580   behavior of silica glass under high-pressure: In-situ Raman study. Journal of Non-

581   Crystalline Solids, 355, 1095–1098.

582   Dziewonski, A.M., and Anderson, D.L. (1981) Preliminary reference Earth model. Physics of the

583   Earth and Planetary Interiors, 25, 297–356.

584   Elliott, S.R. (1991) Origin of the first sharp diffraction peak in the structure factor of covalent

585   glasses. Physical Review Letters, 67, 711–714.

586   Galeener, F.L., and Geissberger, A.E. (1983) Vibrational dynamics in ^{30}Si-substituted vitreous

587   SiO$_2$. Physical review B, 27, 6199–6204.

588   Ghiorso, M.S. (2004) An equation of state for silicate melts. I. Formulation of a general model.

589   American Journal of Science, 304, 637–678.

590   Ghosh, D.B., and Karki, B.B. (2018) First-principles molecular dynamics simulations of

591   anorthite (CaAl$_2$Si2O$_8$) glass at high pressure. Physics and Chemistry of Minerals, 45, 575–

592   587.

593   Ghosh, D.B., Karki, B.B., and Stixrude, L. (2014) First-principles molecular dynamics

594   simulations of MgSiO$_3$ glass: Structure, density, and elasticity at high pressure. American

595   Mineralogist, 99, 1304–1314.

596   Guerette, M., Ackerson, M.R., Thomas, J., Yuan, F., Bruce Watson, E., Walker, D., and Huang,

597   L. (2015) Structure and Properties of Silica Glass Densified in Cold Compression and Hot

598   Compression. Scientific reports, 5, 15343.

599   Guerette, M., Ackerson, M.R., Thomas, J., Watson, E.B., and Huang, L. (2018) Thermally

600   induced amorphous to amorphous transition in hot-compressed silica glass. The Journal of

601   Chemical Physics, 148, 194501.

602   Hemley, R.J., Mao, H.K., Bell, P.M., and Mysen, B.O. (1986) Raman Spectroscopy of SiO$_2$

603   Glass at High Pressure. Physical Review Letters, 57, 747–750.

604   Hirschmann, M.M. (2010) Partial melt in the oceanic low velocity zone. Physics of the Earth and

605   Planetary Interiors, 179, 60–71.

606   Hofler, S., and Seifert, F. (1984) Volume relaxation of compacted SiO$_2$ glass: a model for the

607   conservation of natural diaplectic glasses. Earth and Planetary Science Letters, 67, 433–438.

608   Holtgrewe, N., Greenberg, E., Prescher, C., Prakapenka, V.B., and Goncharov, A.F. (2019)

609   Advanced integrated optical spectroscopy system for diamond anvil cell studies at

610   GSECARS. High Pressure Research, 39, 457–470.

611 Huang, L., Duffrène, L., and Kieffer, J. (2004) Structural transitions in silica glass: Thermo-

612   mechanical anomalies and polyamorphism. Journal of Non-Crystalline Solids, 349, 1–9.

613 Inamura, Y., Katayama, Y., Utsumi, W., and Funakoshi, K.I. (2004) Transformations in the

614   intermediate-range structure of SiO_2 glass under high pressure and temperature. Physical

615   Review Letters, 93, 015501–1.

616 Jing, Z., and Karato, S. (2011) A new approach to the equation of state of silicate melts: An

617   application of the theory of hard sphere mixtures. Geochimica et Cosmochimica Acta, 75,

618   6780–6802.

619 Jing, Z., Yu, T., Xu, M., Chantel, J., and Wang, Y. (2020) High-Pressure Sound Velocity

620   Measurements of Liquids Using In Situ Ultrasonic Techniques in a Multianvil Apparatus.

621   Minerals, 10, 126.

622 Katayama, Y., and Inamura, Y. (2005) Structural studies on liquids and glasses under high

623   pressure and high temperature. Nuclear Instruments and Methods in Physics Research,

624   Section B: Beam Interactions with Materials and Atoms, 238, 154–159.

625 Kawakatsu, H., Kumar, P., Takei, Y., Shinohara, M., Kanazawa, T., Araki, E., and Suyehiro, K.

626   (2009) Seismic evidence for sharp litosphere-astenosphere boundaries of oceanic plates.

627   Science, 324, 499–502.

628 Kono, Y., Park, C., Sakamaki, T., Kenny-Benson, C., Shen, G., and Wang, Y. (2012)

629   Simultaneous structure and elastic wave velocity measurement of SiO_2 glass at high

630   pressures and high temperatures in a Paris-Edinburgh cell. Review of Scientific Instruments,

631   83, 033905.

31

632   Kono, Y., Ohara, K., Kondo, N.M., Yamada, H., Hiroi, S., Noritake, F., Nitta, K., Sekizawa, O.,

633   Higo, Y., Tange, Y., and others (2022) Experimental evidence of tetrahedral symmetry

634   breaking in SiO_2 glass under pressure. Nature Communications, 13, 2292.

635   Kubicki, J.D., Hemley, R.J., and Hofmeister, A.M. (1992) Raman and infrared study of pressure-

636   induced structural changes in $MgSiO_3$, $CaMgSi_2O_6$, and $CaSiO_3$ glasses. American

637   Mineralogist, 77, 258–269.

638   Lange, R.A. (1997) A revised model for the density and thermal expansivity of K_2O-Na_2O-CaO-

639   MgO-Al_2O_3-SiO_2 liquids from 700 to 1900 K: extension to crustal magmatic temperatures.

640   Contributions to Mineralogy and Petrology, 130, 1–11.

641   Li, B., and Liebermann, R.C. (2014) Study of the Earth's interior using measurements of sound

642   velocities in minerals by ultrasonic interferometry. Physics of the Earth and Planetary

643   Interiors, 233, 135–153.

644   Liu, J., and Lin, J.-F. (2014) Abnormal acoustic wave velocities in basaltic and (Fe,Al)-bearing

645   silicate glasses at high pressures. Geophysical Research Letters, 41, 8832–8839.

646   Malfait, W.J., Sanchez-Valle, C., Ardia, P., Médard, E., and Lerch, P. (2011) Compositional

647   dependent compressibility of dissolved water in silicate glasses. American Mineralogist, 96,

648   1402–1409.

649   Malfait, W.J., Seifert, R., Petitgirard, S., Mezouar, M., and Sanchez-Valle, C. (2014) The density

650   of andesitic melts and the compressibility of dissolved water in silicate melts at crustal and

651   upper mantle conditions. Earth and Planetary Science Letters, 393, 31–38.

652   Matsukage, K.N., Jing, Z., and Karato, S. (2005) Density of hydrous silicate melt at the

653   conditions of Earth's deep upper mantle. Nature, 438, 488–491.

654   McMillan, P.F. (1984) Structural Studies of Silicate Glasses and Melts-Applications and

655   Limitations of Raman Spectroscopy. American Mineralogist, 69, 622–644.

656 Meister, R., Robertson, E.C., Werre, R.W., and Raspet, R. (1980) Elastic Moduli of Rock

657   Glasses Under Pressure to 8 Kilobars and Geophysical Implications. Journal of Geophysical

658   Research, 85, 6461–6470.

659 Moulton, B.J.A. (2016) In situ high-pressure structural changes of diopside-anorthite

660   ($CaMgSi_2O_6$-$CaAl_2Si_2O_8$) glasses: A multi-spectroscopic approach. University of Toronto.

661 Moulton, B.J.A., Henderson, G.S., Fukui, H., Hiraoka, N., De Ligny, D., Sonneville, C., and

662   Kanzaki, M. (2016) In situ structural changes of amorphous diopside ($CaMgSi_2O_6$) up to 20

663   GPa: A Raman and O K-edge X-ray Raman spectroscopic study. Geochimica et

664   Cosmochimica Acta, 178, 41–61.

665 Moulton, B.J.A., Henderson, G.S., Martinet, C., Martinez, V., Sonneville, C., and De Ligny, D.

666   (2019) Structure—longitudinal sound velocity relationships in glassy anorthite ($CaAl_2Si_2O_8$)

667   up to 20 GPa: An in situ Raman and Brillouin spectroscopy study. Geochimica et

668   Cosmochimica Acta, 261, 132–144.

669 Mukherjee, G.D., Vaidya, S.N., and Sugandhi, V. (2001) Direct Observation of Amorphous to

670   Amorphous Apparently First-Order Phase Transition in Fused Quartz. Physical Review

671   Letters, 87, 195501.

672 Murakami, M., and Bass, J.D. (2011) Evidence of denser $MgSiO_3$ glass above 133 gigapascal

673   (GPa) and implications for remnants of ultradense silicate melt from a deep magma ocean.

674   Proceedings of the National Academy of Sciences, 108, 17286–17289.

675 Mysen, B.O., and Toplis, M.J. (2007) Structural behavior of Al^{3+} in peralkaline, metaluminous,

676   and peraluminous silicate melts and glasses at ambient pressure. American Mineralogist, 92,

677   933–946.

33

678   Neuville, D.R., De Ligny, D., and Henderson, G.S. (2014) Advances in Raman spectroscopy

679   applied to Earth and material sciences. Reviews in Mineralogy and Geochemistry, 78, 509–

680   541.

681   Reynard, B., Okuno, M., Shimada, Y., Syono, Y., and Willaime, C. (1999) A Raman

682   spectroscopic study of shock-wave densification of anorthite ($CaAl_2Si_2O_8$) glass. Physics

683   and Chemistry of Minerals, 26, 432–436.

684   Richet, P., and Neuville, D.R. (1992) Thermodynamics of silicate melts: configurational

685   properties. In S.K. Saxena, Ed., Thermodynamic data pp. 133–161. Springer, New York,

686   NY.

687   Rigden, S.M., Ahrens, T.J., and Stolper, E.M. (1989) High Pressure Equation of State of Molten

688   Anorthite and Diopside. Journal of Geophysical Research, 94(B7), 9508–9522.

689   Sakamaki, T., Ohtani, E., Urakawa, S., Suzuki, A., and Katayama, Y. (2010) Density of dry

690   peridotite magma at high pressure using an X-ray absorption method. American

691   Mineralogist, 95, 144–147.

692   Sakamaki, T., Wang, Y., Park, C., Yu, T., and Shen, G. (2014a) Contrasting behavior of

693   intermediate-range order structures in jadeite glass and melt. Physics of the Earth and

694   Planetary Interiors, 228, 281–286.

695   Sakamaki, T., Kono, Y., Wang, Y., Park, C., Yu, T., Jing, Z., and Shen, G. (2014b) Contrasting

696   sound velocity and intermediate-range structural order between polymerized and

697   depolymerized silicate glasses under pressure. Earth and Planetary Science Letters, 391,

698   288–295.

699   Sanchez-Valle, C., and Bass, J.D. (2010) Elasticity and pressure-induced structural changes in

700   vitreous $MgSiO_3$-enstatite to lower mantle pressures. Earth and Planetary Science Letters,

701   295, 523–530.

702   Sanloup, C. (2016) Density of magmas at depth. Chemical Geology, 429, 51–59.

703   Sato, T., and Funamori, N. (2010) High-pressure structural transformation of SiO_2 glass up to

704   100 GPa. Physical Review B - Condensed Matter, 82, 184102.

705   Schilling, F.R., Sinogeikin, S. V, Hauser, M., and Bass, J.D. (2003) Elastic properties of model

706   basaltic melt compositions at high temperatures. Journal of Geophysical Research, 108,

707   2304.

708   Schmerr, N. (2012) The Gutenberg Discontinuity: Melt at the Lithosphere-Asthenosphere

709   Boundary. Science, 335, 1480–1483.

710   Seifert, R., Malfait, W.J., Petitgirard, S., and Sanchez-Valle, C. (2013) Density of phonolitic

711   magmas and time scales of crystal fractionation in magma chambers. Earth and Planetary

712   Science Letters, 381, 12–20.

713   Shen, G., Liermann, H.-P., Sinogeikin, S., Yang, W., Hong, X., Yoo, C.-S., and Cynn, H. (2007)

714   Distinct thermal behavior of GeO_2 glass in tetrahedral, intermediate, and octahedral forms.

715   Proceedings of the National Academy of Sciences, 104, 14576–14579.

716   Shimoda, K., Miyamoto, H., Kikuchi, M., Kusaba, K., and Okuno, M. (2005) Structural

717   evolutions of $CaSiO_3$ and $CaMgSi_2O_6$ metasilicate glasses by static compression. Chemical

718   Geology, 222, 83–93.

719   Sonneville, C., Mermet, A., Champagnon, B., Martinet, C., Margueritat, J., de Ligny, D.,

720   Deschamps, T., and Balima, F. (2012) Progressive transformations of silica glass upon

721   densification. The Journal of chemical physics, 137, 124505.

722   Sonneville, C., De Ligny, D., Mermet, A., Champagnon, B., Martinet, C., Henderson, G.H.,

723   Deschamps, T., Margueritat, J., and Barthel, E. (2013) In situ Brillouin study of sodium

35

724   alumino silicate glasses under pressure. The Journal of Chemical Physics, 139, 074501.

725   Stebbins, J.F., Dubinsky, E. V., Kanehashi, K., and Kelsey, K.E. (2008) Temperature effects on

726   non-bridging oxygen and aluminum coordination number in calcium aluminosilicate glasses

727   and melts. Geochimica et Cosmochimica Acta, 72, 910–925.

728   Stern, T.A., Henrys, S.A., Okaya, D., Louie, J.N., Savage, M.K., Lamb, S., Sato, H., Sutherland,

729   R., and Iwasaki, T. (2015) A seismic reflection image for the base of a tectonic plate.

730   Nature, 518, 85–88.

731   Stolper, E., Walker, D., Hager, B.H., and Hays, J.F. (1981) Melt Segregation From Partially

732   Molten Source Regions: The Importance of Melt Density and Source Region Size. Journal

733   of Geophysical Research, 86, 6261–6271.

734   Suito, K., Miyoshi, M., Sasakura, T., and Fujisawa, H. (1992) Elastic Properties of Obsidian,

735   Vitreous SiO_2, and Vitreous GeO_2 Under High Pressure up to 6 GPa. In High-Pressure

736   Research: Application to Earth and Planetary Sciences pp. 219–225. AGU, Washington, D.

737   C.

738   Takei, Y. (2002) Effect of pore geometry on V_P / V_S : From equilibrium geometry to crack.

739   Journal of Geophysical Research, 107, 2043.

740   Tan, C.Z., and Arndt, J. (1999) X-ray diffraction of densifed silica glass. Journal of Non-

741   Crystalline Solids, 249, 47–50.

742   Tange, Y., Nishihara, Y., and Tsuchiya, T. (2009) Unified analyses for P - V - T equation of state

743   of MgO: A solution for pressure-scale problems in high P - T experiments. Journal of

744   Geophysical Research, 114, B03208.

745   Thomas, C.W., and Asimow, P.D. (2013) Preheated shock experiments in the molten

746      $CaAl_2Si_2O_8$-$CaFeSi_2O_6$-$CaMgSi_2O_6$ ternary: A test for linear mixing of liquid volumes at

36

747   high pressure and temperature. Journal of Geophysical Research: Solid Earth, 118, 3354–

748   3365.

749 Tkachev, S.N., Manghnani, M.H., and Williams, Q. (2005) In situ Brillouin Spectroscopy of a

750   Pressure-Induced Apparent Second-Order Transition in a Silicate Glass. Physical Review

751   Letters, 95, 057402.

752 Wang, Y., Rivers, M., Sutton, S., Nishiyama, N., Uchida, T., and Sanehira, T. (2009) The large-

753   volume high-pressure facility at GSECARS: A "Swiss-army-knife" approach to

754   synchrotron-based experimental studies. Physics of the Earth and Planetary Interiors, 174,

755   270–281.

756 Wang, Y., Sakamaki, T., Skinner, L.B., Jing, Z., Yu, T., Kono, Y., Park, C., Shen, G., Rivers,

757   M.L., and Sutton, S.R. (2014) Atomistic insight into viscosity and density of silicate melts

758   under pressure. Nature Communications, 5, 1–10.

759 Williams, Q., and Garnero, E.J. (1996) Seismic Evidence for Partial Melt at the Base of Earth's

760   Mantle. Science, 273, 1528–1530.

761 Wojdyr, M. (2010) Fityk: a general-purpose peak fitting program. Journal of Applied

762   Crystallography, 43, 1126–1128.

763 Wu, L., Yang, D., Xie, H., Li, F., Hu, B., Yu, Y., Xu, W., and Gao, C. (2014) Pressure-induced

764   elastic and structural changes in hydrous basalt glasses : The effect of H_2O on the

765   gravitational stability of basalt melts at the base of the upper mantle. Earth and Planetary

766   Science Letters, 406, 165–173.

767 Xu, M., Jing, Z., Chantel, J., Jiang, P., Yu, T., and Wang, Y. (2018) Ultrasonic Velocity of

768   Diopside Liquid at High Pressure and Temperature: Constraints on Velocity Reduction in

769   the Upper Mantle Due to Partial Melts. Journal of Geophysical Research: Solid Earth, 123,

770   8676–8690.

771 Xu, M., Jing, Z., Van Orman, J.A., Yu, T., and Wang, Y. (2020a) Density of $NaAlSi_2O_6$ Melt at

772   High Pressure and Temperature Measured by In-Situ X-ray Microtomography. Minerals, 10,

773   161.

774 Xu, M., Jing, Z., Bajgain, S.K., Mookherjee, M., Van Orman, J.A., Yu, T., and Wang, Y. (2020b)

775   High-pressure elastic properties of dolomite melt supporting carbonate-induced melting in

776   deep upper mantle. Proceedings of the National Academy of Sciences, 117, 18285–18291.

777 Xu, M., Jing, Z., Yu, T., Alp, E.E., Lavina, B., Van Orman, J.A., and Wang, Y. (2022) Sound

778   velocity and compressibility of melts along the hedenbergite ($CaFeSi_2O_6$)-diopside

779   ($CaMgSi_2O_6$) join at high pressure: Implications for stability and seismic signature of Fe-

780   rich melts in the mantle. Earth and Planetary Science Letters, 577, 117250.

781 Yokoyama, A., Matsui, M., Higo, Y., Kono, Y., Irifune, T., and Funakoshi, K. (2010) Elastic

782   wave velocities of silica glass at high temperatures and high pressures. Journal of Applied

783   Physics, 107, 123530.

784 Zhang, H.L., Hirschmann, M.M., Cottrell, E., Newville, M., and Lanzirotti, A. (2016) Structural

785   environment of iron and accurate determination of $Fe^{3+}/\Sigma Fe$ ratios in andesitic glasses by

786   XANES and Mössbauer spectroscopy. Chemical Geology, 428, 48–58.

787